

# Dispersive shell pellet injection modeling and validation for DIII-D disruption mitigation

Cite as: Phys. Plasmas **28**, 082502 (2021); <https://doi.org/10.1063/5.0054099>

Submitted: 14 April 2021 • Accepted: 13 July 2021 • Published Online: 03 August 2021

 V. A. Izzo



View Online



Export Citation



CrossMark

## ARTICLES YOU MAY BE INTERESTED IN

[Two-photon absorption laser induced fluorescence measurements of absolute neutral deuterium density, temperature, and bulk flow in Proto-MPEX](#)

Phys. Plasmas **28**, 082501 (2021); <https://doi.org/10.1063/5.0054734>

[Characterization of injection and confinement improvement through impurity induced profile modifications on the Wendelstein 7-X stellarator](#)

Phys. Plasmas **28**, 082506 (2021); <https://doi.org/10.1063/5.0047274>

[The relation between the energy conversion rate and reconnection rate in Petschek-type reconnection—Implications for solar flares](#)

Phys. Plasmas **28**, 082103 (2021); <https://doi.org/10.1063/5.0050557>



Physics of Plasmas  
Features in Plasma Physics Webinars

Register Today!

# Dispersive shell pellet injection modeling and validation for DIII-D disruption mitigation

Cite as: Phys. Plasmas **28**, 082502 (2021); doi: [10.1063/5.0054099](https://doi.org/10.1063/5.0054099)

Submitted: 14 April 2021 · Accepted: 13 July 2021 ·

Published Online: 3 August 2021




View Online



Export Citation



CrossMark

V. A. Izzo<sup>a)</sup> 

## AFFILIATIONS

Fiat Lux, San Diego, California 92101, USA

<sup>a)</sup> Author to whom correspondence should be addressed: [izzo@fusion.gat.com](mailto:izzo@fusion.gat.com)

## ABSTRACT

Dispersive shell pellet injection for disruption mitigation on the DIII-D tokamak is modeled with the 3D MHD code NIMROD. The simulations attempt to reproduce as closely as possible a pellet velocity scan that was performed on the DIII-D tokamak [Hollmann, *et al.*, Phys. Rev. Lett. **122**, 65001 (2019)]. This scan involved injecting a hollow diamond shell filled with boron dust that is released in the core of the plasma. Trends that are reproduced in the simulation include improved mitigation, reduced plasma current spike amplitude, and increased likelihood of hot-tail runaway electron production with increased pellet speed. The simulations provide additional physics insight into these findings. Limitations of the present model and requirements for a predictive model are discussed.

Published under an exclusive license by AIP Publishing. <https://doi.org/10.1063/5.0054099>

## I. INTRODUCTION AND BACKGROUND

It is a truth universally acknowledged that success of the ITER mission depends on a reliable system to mitigate those disruptions that cannot be avoided.<sup>1</sup> Shattered pellet injection (SPI), first demonstrated on the DIII-D tokamak,<sup>2</sup> and since deployed on other devices,<sup>3–6</sup> is the basis for the design of the ITER Disruption Mitigation System (DMS). However, SPI is not certain to solve every disruption challenge, and the conversion of current carried by thermal electrons to a high energy beam of relativistic runaway electrons (REs) remains particularly worrisome, so alternate methods of disruption mitigation continue to be pursued. Among these, dispersive shell pellet (DSP) injection has been demonstrated on DIII-D<sup>7</sup> by injecting hollow spherical diamond shells filled with boron dust into the tokamak at sufficient velocity to ablate the carbon shell gradually in the edge and release the boron payload near the center. The goal of this method is to cool the plasma from the inside out, thus radiating the lion's share of the core thermal energy while conducting minimal heat to the divertor. The intact flux surfaces in the unperturbed edge might also permit a slower rate of radiation cooling in the core—with lower Z impurities—avoiding the production of RE seeds by the hot-tail mechanism.

In the DIII-D DSP experiments,<sup>7</sup> pellets were injected with velocities ranging from  $\sim 100$ – $230$  m/s. Several clear trends were observed as pellet velocity was increased, including decreased amplitude of the plasma current spike, shorter current quench duration, reduced heat fluence at the outer-divertor strike-point, and increased hard-x-ray

(HXR) signal, indicating a “prompt-loss” of REs generated during the TQ. The goal of the work described here is to determine which of these trends can be reproduced by 3D MHD modeling of DSP into DIII-D, both to gain physics insight into these trends—and DSP in general—and to understand what deficiencies exist in the model that need to be addressed in order to enable predictive modeling of DSP into ITER or other future tokamaks.

3D MHD modeling of disruption mitigation, incorporating a radiating impurity species, was first performed with NIMROD to model massive gas injection (MGI) on Alcator C-Mod<sup>8,9</sup> and subsequently on DIII-D.<sup>10</sup> Among the key physics insights gained from this modeling was the role of the  $n = 1$  modes in determining the asymmetry of radiated power,<sup>10,11</sup> with experiments subsequently showing similar effects.<sup>12</sup> NIMROD also includes a model for RE test-particle drift-orbits, which was used to predict a very pessimistic  $R^3$  machine-size scaling for the confinement of runaway electron seeds.<sup>13</sup> A radiating impurity model for disruption mitigation has also been incorporated into two other 3D MHD codes: M3D-C1,<sup>14,15</sup> which has been carefully benchmarked with NIMROD and also allows for a two-temperature model for the thermal quench, and JOREK,<sup>16</sup> which has also included a RE test-particle model.<sup>17</sup> Considerable effort has been made recently to model SPI<sup>16,18–20</sup> as the primary strategy for ITER.

Modeling of DSP with NIMROD has previously focused on the dynamics of an inside-out thermal quench, with a model for the shell either neglected<sup>21</sup> or considerably simplified.<sup>22</sup> Here, we present a more detailed effort to reproduce DIII-D experimental trends. The

model itself is improved, with the addition of a non-constant shell ablation model, calibrated to experiments, and boron atomic data for more accurate modeling of the payload (both described in Sec. II). Some of the physics parameters are pushed closer to realistic values, including the use of realistic Spitzer resistivity with no cutoff at high temperature, and sensitivities to viscosity and source localization are studied (Sec. III E). The main thrust of the simulations (Secs. III A–III D) is a scan over pellet velocity for three otherwise identical simulations and a comparison with the experimental pellet velocity scan performed by Hollmann.<sup>7</sup> In Sec. IV, we provide a summary of where the model succeeds and fails. Three experimental trends vs pellet speed are reproduced by the simulations. First, the TQ mitigation efficiency, indicated by the radiated power fraction and evidenced experimentally by the divertor heat fluence, increases with pellet speed. Second, the appearance of RE seeds only for fast pellets in DIII-D is consistent with the variation in core temperature evolution in the simulations. Third, the decrease in the plasma current spike amplitude with faster pellets is reproduced and explained in terms of the evolution of poloidal flux. We finally discuss what insight into the experimental trends is gained from the modeling and consider the requirements for predictive DSP model in light of the results.

## II. COMPUTATIONAL MODEL

### A. Code description

The 3D extended-MHD simulations described herein are performed with the NIMROD code,<sup>23</sup> including extensions for impurity radiation<sup>11</sup> and runaway electron (RE) test-particles.<sup>13</sup> These models have been described extensively in the references given, but briefly, the model is single-fluid MHD, having a single temperature and single fluid velocity. The densities of each impurity charge state, and the main deuterium ion density, are evolved by separate continuity equations (six additional continuity equations for boron, plus seven for carbon), with ionization and recombination rates calculated for transitions between charge state populations. The energy equation includes cooling due to ionization, and recombination, bremsstrahlung, and line radiation. The “pellet” in the simulation is simply a volumetric source of neutral impurity density having a specified temporal and spatial distribution whose total rate (atoms/s) is given by the pellet ablation rate (discussed in Sec. II B). The (moving) region in which the neutral atoms are deposited is governed by the same equations as the rest of the plasma, and the solid pellet itself is essentially a phantom—only the ablated material from the pellet enters the simulation. With a single temperature model, energy conservation dictates that the plasma also cools instantaneously by dilution as the density rises due to the added neutrals and due to ionization. As the MHD equations are advanced, drift orbits are calculated for runaway electron test-particles, with equations for parallel and total momentum in addition to three spatial evolution equations. The momentum evolution includes acceleration due to the electric field and drag due to small-angle collisions, and synchrotron and bremsstrahlung radiation. Pitch-angle scattering by large-angle collisions is not included. The test-particles have no effect on the MHD fields and are initialized at relativistic energies—no RE generation model is included.

The radiation and ionization rates originally incorporated into NIMROD are ADPACK rates taken from the KPRAD code,<sup>24</sup> including atomic data for He, Be, C, N, Ne, and Ar. These rates are non-equilibrium Corona rates, meaning (as stated above) radiation from

each impurity charge state is calculated separately, and a low-density regime is assumed. The total line radiation in the energy equation is then given as a sum over radiation from every impurity charge state  $Z$ :  $P_{rad} = \sum_z n_e n_z L_z$ , where  $n_z$  is the density of a particular charge state, and the coefficient  $L_z$  from KPRAD is dependent only on  $T_e$ . Since boron is the payload species for the DIII-D DSP experiments modeled here, and no boron data were previously included in the code, we have added atomic data for both line emission from excitation and electron impact ionization<sup>25,26</sup> taken from OPEN-ADAS.<sup>27</sup> The ADAS rates are calculated using the collisional-radiative model, which should approach the Corona model at low density. In principle, the coefficients  $L_z$  from this model are dependent on both  $T_e$  and  $n_e$ , and the coefficients in the file Ref. 25 are presented in a 2D table. However, in reality, this particular data file contains no variation with density over the five orders of magnitude range given, so that it can also be represented simply as an  $L_z(T)$  function for each charge state without any reduction of the data and used in the code in an identical manner to the KPRAD data. It is desirable to perform basic checks of these new data and compare with existing data in the code, so a set of three short simulations was run in which a toroidally symmetric source of neutral impurities, centered on-axis, is deposited in a DIII-D equilibrium during a time window of 0.1 ms, after which the impurity source is turned off. We compare simulations with an identical number of atoms added at an identical rate for Be, B, and C impurities, where the Be and C simulations use the existing ADPACK data in NIMROD and the B simulation uses the newly added B OPEN-ADAS data. Figure 1 shows the number of added impurities and electrons and the total line radiation for each simulation. Each case radiates strongly as new neutral impurities are added then falls off sharply when the injection ceases. The impurities become highly ionized but not fully stripped in every case, as indicated by the ratio of added electrons to impurity ions. That the B results remain bounded by the Be and C results at all times indicates that this OPEN-ADAS data falls very reasonably in line with ADPACK data already included in the code.

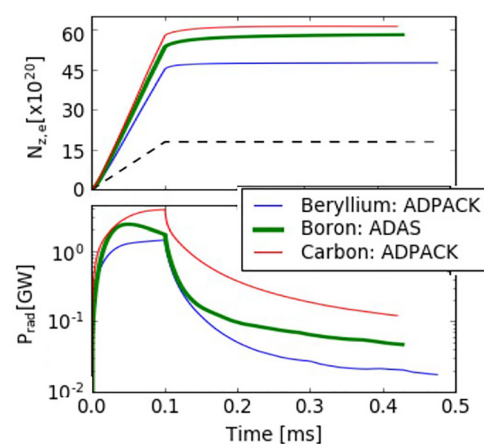


**FIG. 1.** Test simulation to compare new B atomic data to Be and C data already in the code. (Upper) added impurity atoms, which is the same for all three simulations (dashed) and added electrons for each species vs time. (Lower) total impurity line radiation for each species vs time.

**B. Ablation model**

Each simulation presented here models the injection of a carbon shell containing a boron payload, in accord with DIII-D DSP experiments. The impurity deposition model consists of a source of neutral impurities traveling at a constant rate along the outer midplane of the equilibrium from the edge to the core. The poloidal distribution of the impurity source is a circular Gaussian distribution and the toroidal distribution is a von Mises distribution (circular normal distribution) as described in Ref. 22. In every simulation, the total quantity of shell carbon deposited is  $3.01 \times 10^{20}$  atoms, and the boron payload comprises  $1.17 \times 10^{21}$  atoms, the nominal shell and payload quantities from the DIII-D experiments. As the source travels from the edge at the prescribed velocity, the carbon shell material is first deposited at a rate governed by the local plasma temperature and density (due to the thin shell, the radial dependence of the ablation rate is ignored and absorbed into the coefficient). The ablation rate used here is

$$G(\text{atoms/s}) = 1.44 \times 10^{11} T^{5/3} n^{1/3}. \tag{1}$$

The temperature and electron density are in eV and  $\text{m}^{-3}$ , respectively. The exponents for this model are based on the ablation model for hydrogenic pellets of Parks.<sup>28</sup> Because that model gives much too high ablation rates for the diamond shell, the value of the coefficient is chosen (by some trial and error) so that a 230 m/s pellet ablates the entire shell and releases its payload at  $r/a = 0.25$  in the simulation. This target release location is based on the results reported for a 230 m/s pellet in Ref. 7 for which the payload is released at  $r/a = 0.25$  and disappears at  $r/a = 0.15$ . Having calibrated the model to this pellet velocity, the velocity scan is then carried out with the same ablation coefficient for every case. Ideally, a theoretical model would eventually replace this *ad hoc* ablation model, but we will see in Sec. III that it is sufficient to reproduce several experimental trends.

Once the total shell mass has been deposited, the source species switches to the boron payload material, which is deposited with the same spatial dependence at a constant rate determined by the total payload quantity, the specified distance over which to release the payload, and the pellet speed. The source velocity remains constant, so that the effect of payload slowing after the shell breaks open is not accounted for, but the distance over which the payload is released is matched to the experiment ( $r/a = 0.1$ ). An example of the total deposited impurity quantity vs time for a simulation with a 230 m/s pellet is seen in Fig. 2. The nonlinear behavior of the shell ablation reflects both the temperature and density profiles of the target equilibrium, and (as will be discussed further in Sec. III) the evolution of those profiles in direct response to ablated impurities and to the onset of unstable MHD modes, which causes the slowing of the ablation rate just prior to payload release.

**C. Simulation parameters**

Each of the simulations described here begins with a 1.46 MA lower-single-null diverted DIII-D equilibrium, having 1.05 MJ of stored thermal energy, an edge safety factor  $q_{95} = 3.1$ , and a safety factor on axis  $q_0 = q_{\text{min}} = 1.05$ . The poloidal plane is discretized with a resolution of 40 (radial)  $\times$  56 (poloidal) finite elements, with fifth-order polynomial basis functions within each element. The toroidal direction is represented by Fourier components  $n = 0-10$ . In every simulation, realistic temperature- and  $Z_{\text{eff}}$ -dependent Spitzer resistivity

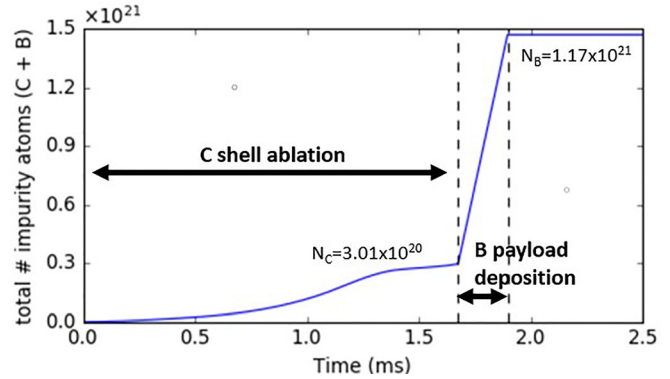


**FIG. 2.** Example neutral deposition vs time result for a single simulation (230 m/s pellet), with the C shell ablation governed by Eq. (1) and a constant payload deposition rate.

values are used, with no cutoff at high temperature, with an expression given as  $\eta[\Omega\text{m}] = 3.393 \times 10^{-4} Z_{\text{eff}} T_e^{-3/2}$ . Viscosity values given in Table I are coefficients of both the parallel ( $\vec{\Pi} = -3\rho\nu_{\parallel} / 2 [\hat{\mathbf{b}} \cdot \vec{W} \cdot \hat{\mathbf{b}}] [\hat{\mathbf{b}}\hat{\mathbf{b}} - \vec{I} / 3]$ ) and isotropic ( $\vec{\Pi} = -\rho\nu_{\text{iso}} \vec{W}$ ) viscosity (with  $\vec{W}$  strain-rate tensor). The large values chosen may produce strong viscous damping of MHD activity and are chosen by necessity for reasons of numerical stability. With realistic resistivity, the highest viscosity gives values of the Prandtl number of  $6 \times 10^5$  in the initially hot core or 10 in the coldest regions of the post-TQ plasma. These are not atypical values in comparable NIMROD simulations. For instance, the SPI simulations reported in Ref. 19 quote a Prandtl number on-axis of  $10^5$  but with resistivity enhanced by two orders of magnitude, so that we may infer viscosity values roughly an order of magnitude higher than used in the present work. The effects of viscosity will be revisited in the discussion section. The toroidal peaking of the neutral source can be most intuitively characterized by the source toroidal peaking factor (STPF) which is the toroidal maximum of the neutral source divided by the toroidal average (also used to characterize radiation peaking) and for these simulations has a moderate value of STPF = 1.7. The values of parallel and perpendicular thermal conduction are constant and given as  $\kappa_{\parallel} = 10^8 \text{ m}^2/\text{s}$  and  $\kappa_{\perp} = 2.0 \text{ m}^2/\text{s}$ , respectively. A non-constant rate of parallel thermal conduction,

**TABLE I.** Varied parameters for seven simulations. Cases 1.0, 2.0, and 3.0, scanning only over pellet velocity, are the primary cases discussed in Sec. III.

Case label	Pellet velocity	Viscosity	Poloidal source localization (HWHM)
Case 1.0	230 m/s	520 $\text{m}^2/\text{s}$	0.083 m
Case 2.0	175 m/s	520 $\text{m}^2/\text{s}$	0.083 m
Case 3.0	115 m/s	520 $\text{m}^2/\text{s}$	0.083 m
Case 1.1	230 m/s	260 $\text{m}^2/\text{s}$	0.083 m
Case 1.2	230 m/s	130 $\text{m}^2/\text{s}$	0.083 m
Case 3.1	115 m/s	260 $\text{m}^2/\text{s}$	0.083 m
Case 3.2	115 m/s	520 $\text{m}^2/\text{s}$	0.042 m

which should vary as  $T^{5/2}$ , can make the temperature advance numerically intractable when steep gradients occur in regions of stochastic fields. The primary consequence of the constant value chosen will be to overestimate parallel transport in cold regions of the plasma. Because the plasma stochasticizes from the inside out, this approximation should have less effect on the fraction of energy conducted to the wall than in the case of SPI simulations, for instance, but could affect the rate at which the local cooling in the center spreads outward. For numerical stability purposes, an artificial particle diffusion of  $0.5 \text{ m}^2/\text{s}$  is included for all species. The payload is dispersed over a width of  $r/a = 0.1$  in every case, based on the single experimental case to which the ablation model is calibrated, with the constant payload delivery rate determined by the total payload quantity and the interval over which it is delivered. This model for the payload delivery does not account for differences as the pellet speed is varied or slowing down of the payload after release. The primary parameter that is scanned for this study is the pellet velocity, with values of 230, 175, and 115 m/s modeled with otherwise identical parameters, and this comparison will be the focus of parts A–D of Sec. III. For specific cases, additional simulations are run to examine the effects of other parameters, namely, viscosity and poloidal source localization. Results of these simulations will be considered in Sec. III E. The table below lists all parameters that are varied over the total set of cases discussed.

### III. SIMULATIONS RESULTS

#### A. Overview

For cases 1.0, 2.0, and 3.0, we compare the time histories of the impurity source rate, total plasma current, total stored thermal energy, and  $n = 1$  mode amplitudes in Fig. 3 (for clarity,  $n = 2$ – $10$  mode amplitudes are plotted only for case 1.0;  $n = 1$  is the dominant mode at all times in every simulation). Each case is characterized by a loss of just under 20% of the stored thermal energy prior to payload release (pre-TQ phase) and a TQ time between 1.5 and 2.0 ms from payload release until the plasma current spike, which occurs once nearly all the stored thermal energy is lost. The  $n = 1$  mode is perturbed directly by the pellet source beginning in the pre-TQ and has multiple peaks but reaches its largest amplitude just before the  $I_p$  spike. We note that the timing of the 175 m/s case is much closer to that of the 230 m/s case than that of the 115 m/s case. On the other hand, if we plot the locations of the payload release (Fig. 4), we find that the 115 and 175 m/s pellets release their payloads at nearly identical locations ( $r/a = 0.39$ ), and only the 230 m/s pellet penetrates further to the core ( $r/a = 0.25$ ). The deposition vs  $r/a$  for the three primary cases is also compared with the other four simulations in Fig. 4, which will be discussed more in Sec. III E. In each simulation of the primary pellet velocity scan, the payload is released inside of the  $q = 1.5$  surface. The strong temperature dependence of the ablation rate produces the highly nonlinear dependence of the payload release location on pellet velocity. The pellet ablation is very weak in the edge then begins to increase, only to slow down again in every case before payload release [Fig. 3(a)]. This slowing of the ablation rate results from the growth of the  $n = 1$  mode in the core, which distorts and shifts the hot core away from the incoming pellet. This can be seen in the field line Poincaré plot and temperature contours at the pellet toroidal location before payload release for case 1.0 shown in Fig. 5. In MGI simulations of DIII-D, it was previously observed that the phase of the  $m/n = 1/1$  mode in the core aligns such that the heat flux associated with the mode is away

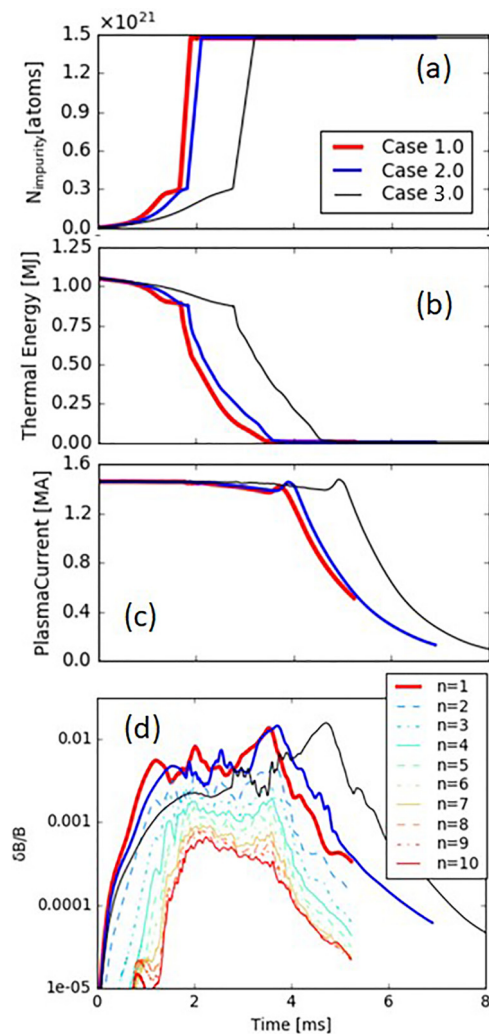


**FIG. 3.** Overview of thermal and current quenches for three simulations with different pellet velocities: case 1.0 (230 m/s), case 2.0 (175 m/s) and case 3.0 (115 m/s); (a) total deposited impurities (C + B), (b) stored thermal energy, (c) plasma current, and (d)  $n = 1$  mode amplitudes ( $n = 2$ – $10$  plotted only for case 1.0).

from the incoming impurity source,<sup>10</sup> which is consistent with the present finding. We also note from Fig. 5 that, while the shell material itself is sufficient to trigger some pre-TQ unstable mode growth and produce a stochastic region near the core, this remains surrounded by a large mantle of good flux surfaces.

Time traces of radiated power and Ohmic heating are compared in Fig. 6 for the fastest and slowest pellet cases (various metrics for all three will be compared in Sec. III B). In addition to impurity line radiation, which is the dominant radiation term, recombination radiation becomes significant for a short interval after the initial ionization of the payload and subsequent local cooling of the plasma. Although included in the calculation, bremsstrahlung radiation is negligible and not plotted. In each case, we see a narrow spike in radiation when the payload is first released—which is much higher for the 230 m/s pellet—and eventually a more steady-state level of radiation that is

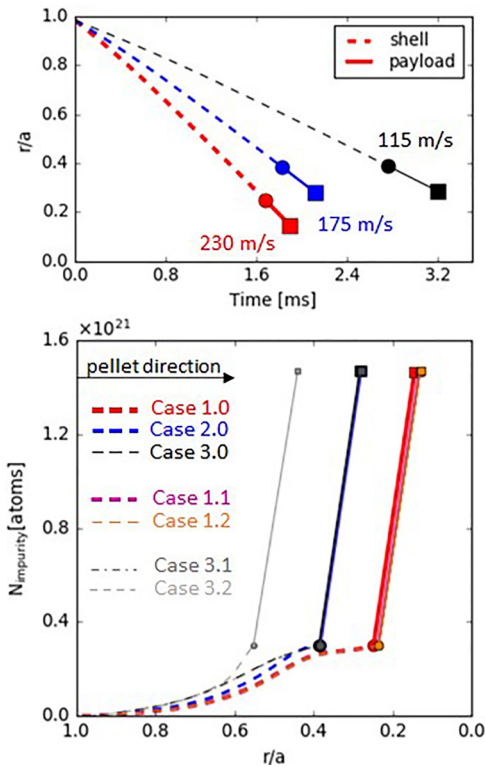


**FIG. 4.** (Upper) variation of time and location for payload release with different pellet velocities for cases 1.0, 2.0, and 3.0. (Lower) a comparison of the cumulative spatial deposition of impurity atoms vs  $r/a$  for all seven cases with broken lines indicating carbon deposition and solid indicating boron deposition. Cases 1.1 and 1.2 with varying viscosity lie almost on top of each other and very near to case 1.0. Likewise, case 3.1 with lower viscosity lies almost on top of case 3.0 (both have a different shell deposition profile but nearly the same payload deposition as case 2.0). Case 3.2 with more localized deposition has an earlier payload release as will be discussed in Sec. III E.

around  $\sim 0.7$  GW in both cases. Between the spike and the eventual steady state, only the slow pellet case has a short interval of lower radiation  $\sim 0.4$  GW. Both the smaller initial spike and the low radiation interval for case 3.0 stem from the fact that the core plasma begins at a higher temperature and cools initially to a higher temperature than case 1.0, which will be further discussed in the section on runaway electrons (Sec. III C). As the thermal quench proceeds, Ohmic heating grows to eventually match radiated power (with the peak closely corresponding to the time of the  $I_p$  spike) and the two curves fall off together as the CQ proceeds. The total electron quantity added by the impurities is also plotted in Fig. 6 and compared to the impurity quantity. In each case, the payload becomes highly ionized at first then the electron number falls off, with the  $B^{+1}$  eventually becoming the dominant charge state. The payload released closer to the core becomes less ionized and recombines more quickly than the payload released at larger  $r/a$ . This is also explained by the counter-intuitive fact that the initial temperature at the payload is lower and drops more quickly for the deeper penetrating pellet, as discussed in more detail in Sec. III C.

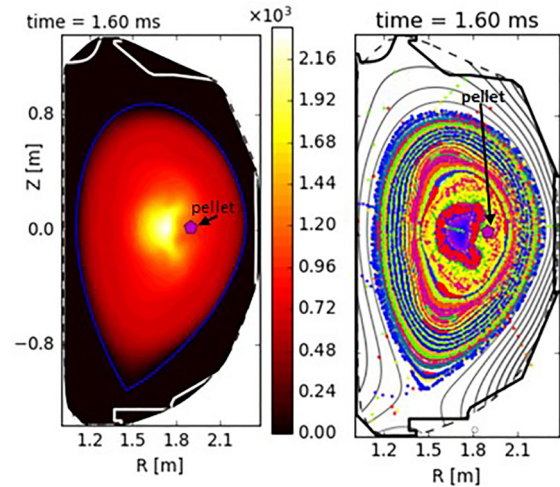


**FIG. 5.** Distortion of core due to  $n = 1$  for case 1.0 at 1.6 ms (slightly prior to payload release). Magenta pentagon shows pellet location at this time. (left) Temperature contours (eV), (right) magnetic field line Poincare plot. The dashed line is the simulation boundary, but the actual DIII-D limiter shape is also plotted as a solid line.

### B. Thermal quench mitigation metrics

A successful thermal quench mitigation scheme should radiate the largest possible fraction of the stored thermal energy to reduce the fraction that is conducted to the divertor. In the DIII-D velocity scan experiment in Ref. 7, the mitigation efficacy was assessed by comparing the heat fluence measured at the divertor inner-strike-point, and it was found that this was reduced at higher pellet velocities, indicating better mitigation. In the simulations, the most straightforward metric for comparison is the radiated energy fraction. The energy accounting for case 1.0 shown in Fig. 7 illustrates the definition of this metric. As the impurities are deposited, stored thermal energy goes both into radiation, which is lost from the system, and ionization of the

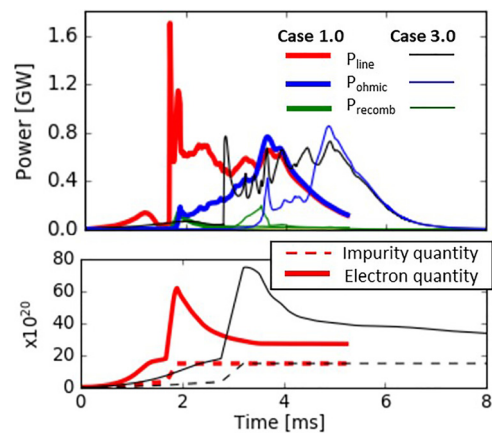


**FIG. 6.** A comparison of thermal quench radiation and ionization/recombination characteristics for a fast and slow pellet; (upper) radiated power (line and recombination radiation) and Ohmic heating power for cases 1.0 and 3.0 and (lower) total added electrons and impurities for the same two cases.

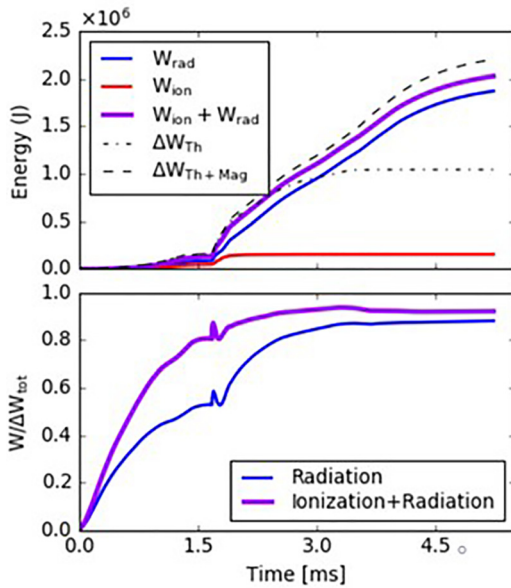


**FIG. 7.** An illustration of the calculation of radiated energy fraction for case 1.0; (upper) a comparison of energy into ionization, radiation (excluding recombination), and the total of the two, with thermal energy lost and total energy lost from the system; (lower) the ratio of total radiated energy (including recombination), and of energy into ionization plus radiation (w/o recombination), to the total thermal plus magnetic energy lost.

impurities. The latter energy can later be lost in the form of recombination radiation. Therefore, we can sum just the radiation terms, including recombination radiation, to produce total radiated power, or we can sum all radiation terms except recombination, plus ionization energy. The latter sum will be higher, while some impurities remain ionized and give the fullest accounting of energy that is not conducted to the divertor, so we use the sum of radiation and ionization to calculate the radiated energy fraction. The upper part of Fig. 7 compares the total of energy into ionization and radiation with the loss of just thermal energy and of thermal plus magnetic energy from the system. After the thermal quench, when radiation and Ohmic heating balance, all the energy being radiated is magnetic energy. The lower part of Fig. 7 is the calculation of the radiated energy fraction  $f_{rad}$  as the ratio of the radiation and ionization energy to the total change in energy. This reaches a plateau value in the CQ, which is considered the value of  $f_{rad}$  for the simulation. Also plotted is the slightly lower curve obtained by summing all radiation terms, including recombination, but excluding ionization.

A comparison of radiated energy fraction for three pellet velocities in Fig. 8 shows a trend of improved mitigation with increasing velocity. We note that the radiation fraction is quite high in every case, with the lowest value exceeding 85%, but only the fastest pellet exceeds the 90% target threshold established for the ITER DMS.<sup>1</sup> The radiation fraction, along with the other trends plotted in Fig. 7, shows a surprisingly linear trend with pellet velocity, given that the shell ablation is so nonlinear and that the 115 and 175 m/s pellets have identical payload release locations. A less favorable trend is the approximately linear increase in maximum radiated power with pellet velocity although we saw from the comparison of two cases in Fig. 6 that this maximum

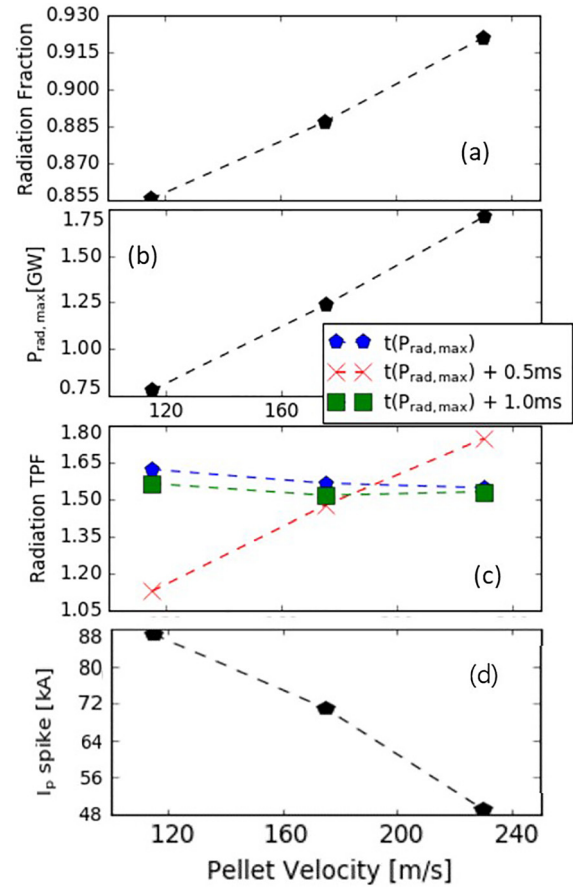


**FIG. 8.** Major trends as a function of pellet velocity. (a) Radiated power fraction, (b) maximum radiated power, and (c) radiation toroidal peaking at three times, and (d)  $I_p$  spike amplitude, compared for cases 1.0, 2.0, and 3.0.

corresponds to a narrow spike at the time of payload release, whereas most of the stored thermal energy is lost in the more steady-state phase of the radiation, at a comparable level in each case. Figure 8(c) compares the toroidal radiation peaking factors (TPF = maximum/average) at three times: the time of the maximum radiated power, and 0.5 and 1.0 ms after the maximum. Recall that the neutral source itself has a TPF of only 1.7, and this is likely the dominant factor in determining the radiation TPF values around 1.5 observed in the simulation (a DSP simulation in Ref. 22 with a source TPF of 3.7 had a radiation TPF of 3.3 at the time of maximum radiated power), such that this finding cannot be considered predictive for a more localized pellet. The TPF values during the initial radiation peak and after 1 ms are all quite similar, but we do observe an opposing trend in the intermediate time when the TPF temporarily drops for the slowest pellet and rises for the fastest pellet. This occurs during the intermediate low radiation phase for case 3.0 that does not occur in case 1.0 (Fig. 6), which will be further discussed in the runaway electron section (Sec. III C).

### C. Runaway electrons

The primary observation concerning runaway electrons in the DIII-D experiments was that only the fastest pellet (230 m/s) had a

measurable “prompt loss” of runaway electron seeds at the end of the TQ,<sup>7</sup> indicated by hard-x-rays (HXR) produced when  $\sim 1$  MeV or greater REs strike the DIII-D wall. To understand this result, we wish to examine both how RE generation and RE loss may differ for different pellet velocities. The NIMROD RE test-particle model contains no model for RE generation; it merely seeds test-particles above the runaway threshold to study their confinement. We can nonetheless examine the evolution of the temperature profiles in the simulations to gain some insight into how runaway electron generation may vary over the set of simulations. In DIII-D, the Dreicer mechanism<sup>29</sup> of RE seed generation has been estimated to be insufficient, while the hot-tail mechanism<sup>30</sup> predicts much larger seeds.<sup>31</sup> Thus, it seems that the conditions for RE generation during a DIII-D TQ are as follows: condition 1) a drop in temperature that is fast enough compared to the temperature equilibration time to produce a non-Maxwellian electron distribution (i.e., a hot-tail), and condition 2) a final state at the end of that temperature drop in which  $E > E_c$ , where  $E_c$  is the critical electric field,<sup>29</sup> below which no runaways are possible.

Examining temperature profiles over a range of 0.3 ms beginning just prior to payload release for cases 1.0 and 3.0 (Fig. 9), we see that rapid cooling occurs in the early phase of this time interval and has slowed considerably by the end. The cooling rates are comparable, but

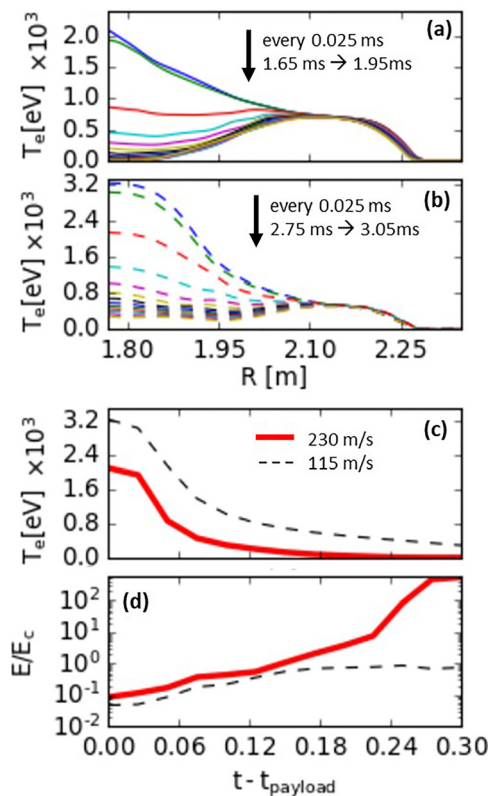


**FIG. 9.** Comparison of cooling in the core after payload release for a slow and fast pellet, illustrated by temperature profiles at the outboard midplane beginning at the time of the payload release for (a) case 1.0 and (b) case 3.0. (c) Comparison of  $T$  on axis over the 0.3 ms interval after payload release for the two cases, and (d) comparison of  $E/E_c$ .

at the end of this interval, the temperature on axis [Fig. 9(c)] for case 1.0 is  $\sim 1$  eV, whereas it remains  $> 200$  eV for case 3.0. This is due in part to the lower starting temperature in case 1.0, where the core is pre-cooled by dilution due to shell electrons in the core. The concentration of the more centered payload within a smaller volume of flux surfaces is also important in determining the lower final temperature. We calculate the ratio of the electric field to the critical field [Fig. 9(d)], using the approximation  $E_c = 0.12 n_e(\text{m}^{-3})/10^{20}$ . While  $E/E_c$  in case 3.0 remains just below unity after 0.3 ms, it exceeds 600 in case 1.0. The temperature on axis does eventually drop to the  $\sim 1$  eV range for case 3.0, such that  $E$  eventually exceeds  $E_c$  but this occurs over an additional time interval exceeding 0.5 ms, and the hot-tail mechanism depends on the fast cooling rate.

Very similar time scales were considered in a careful comparison of DIII-D RE seed levels with analytic seed generation estimates by Hollmann,<sup>31</sup> in which a temperature decay time of 0.3 ms for DIII-D experiments with Ar pellet injection was observed. It was noted that this was comparable to the initial electron temperature equilibration time of 0.1–0.3 ms so that the steady-state Dreicer assumption is not valid, but the hot-tail assumption of cooling faster than the equilibration time is only marginally applicable, perhaps explaining overestimates of the observed seed by the analytic hot-tail model of Smith.<sup>30</sup> Thus, we can suppose that the initial cooling rate in the simulations is “fast-enough” (condition 1) in that it matches the rate that is actually seen to produce seeds in DIII-D experiments. Clearly condition 2 ( $E > E_c$ ) is only met in case 1.0, with plenty of time for the population to return to a Maxwellian before  $E$  eventually exceeds  $E_c$  in case 3.0. Therefore, the temperature profile evolution in the simulations is quite consistent with the production of RE seeds for a pellet speed of 230 m/s, but not for a pellet speed of 115 m/s, as was observed in the experiments.

Losses of runaway electron seeds (assuming they are generated in each case) are found to increase somewhat with increasing pellet velocity (Fig. 10). Each simulation begins with 7020 RE test-particles seeded randomly over the closed flux region, having an average energy of 1 MeV with a narrow Gaussian spread (0.1 MeV half-width) about the average. Note that since we only expect RE generation in the core (in one case), the initialization of REs over the whole cross section will not give us an estimate of the true percentage that would be lost experimentally, only the fraction of the poloidal cross section in which REs that are generated would remain confined. The initial average pitch angle is 0.4 with a Gaussian half-width of 0.1 about the average. Since no pitch-angle scattering term is included, pitch decreases as the REs are accelerated to higher energy. In case 1.0, 100% of the RE test particles are lost to the outer divertor strike point due to field stochasticity by 4.0 ms, just at the start of CQ, before any significant avalanching would occur. By contrast, cases 2.0 and 3.0 each have a small population of test particles in the core (5 and 8, respectively), comprising  $\sim 0.1\%$  of the initial seeds, that survive into the CQ and are eventually lost to the outer-midplane due to curvature drift as their energies become large and the current decays. Under real conditions, these surviving test particles could continuously produce new low energy REs by knock-on, and the exponentially growing RE population could sustain the plasma current, but these effects are not incorporated into the test particle model.

We will see in Sec. III D that the final peak in the  $n = 1$  mode amplitude has a radial mode structure that is largest in the outer region

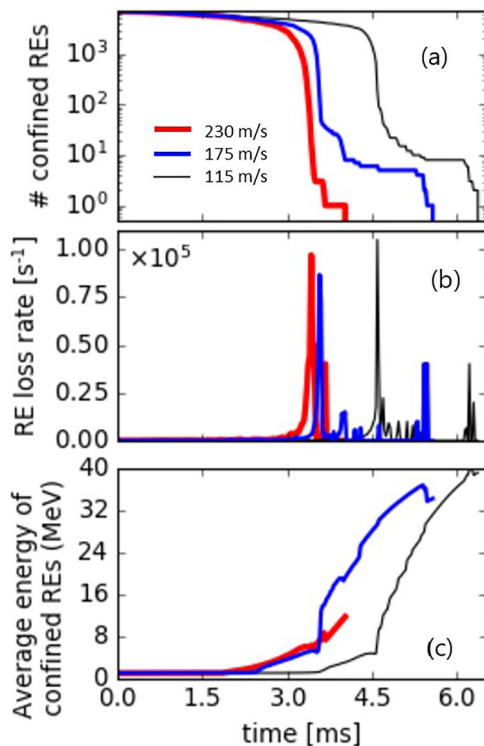


**FIG. 10.** (a) Number of confined RE test particles (on a log scale) vs time for cases 1.0, 2.0, and 3.0. (b) RE loss rate ( $N_{RE}[dN_{RE}/dt]^{-1}$ ), and (c) average RE energy.

of the plasma and small in the core [Figs. 12(c) and 12(d)]. At the time of the  $n = 1$  mode peak, when the edge of the plasma is most strongly stochastic (indicated by the sparsity of points and short connection lengths on the Poincaré plot in Fig. 11), all cases have some small regions of good flux surfaces near the magnetic axis. However, we note that the large majority of REs are lost prior to the final  $n = 1$  peak. We compare the RE distribution at two times for cases 1.0 and 3.0, where the first time slice is chosen to have as close as possible to 100 REs remaining confined, and the second is the time of the  $n = 1$  peak amplitude (Fig. 11). These times fall closer together for case 3.0, the first being 0.1 ms prior to the  $n = 1$  peak, whereas the time of  $\sim 100$  remaining REs is 0.15 ms prior to the peak in case 1.0. This occurs because, preceding the  $n = 1$  mode peak, case 3.0 confines REs better in the core due to a persistent closed flux region. By the time of the  $n = 1$  mode peak, the residual population of confined REs is very clustered in the core. On the other hand, REs are lost across the entire cross section before the  $n = 1$  mode peak in case 1.0 due to greater core stochasticity. When a core of good flux surfaces re-forms as the large  $n = 1$  appears in the edge, no significant RE population remains in the core. REs near the axis are also accelerated to higher energy in case 3.0, which can improve confinement with respect to magnetic perturbations.<sup>32</sup>

#### D. Plasma current spike

Defined as the difference in current between the local maximum and the preceding local minimum, the amplitude of the plasma

current spike also shows an almost linear trend with pellet velocity [Fig. 8(d)]. The increase in  $I_p$  spike amplitude as pellet velocity decreases is consistent with what was observed on DIII-D<sup>7</sup> although the trend appears more step-like than linear in the experiments, with the intermediate velocity pellet having comparable amplitude to the higher velocity pellets. The lowest simulated value is very similar to the experimentally measured amplitude for the 230 m/s pellet, while the highest is a bit lower than the largest measured values of  $\sim 120$  kA. The observed stepwise behavior raises the question of whether some qualitatively different physics is in play to produce the larger current spikes seen for the slower pellets. We will compare here in detail the current density evolution and related MHD activity for the 49 kA plasma current spike in case 1.0 and the considerably larger 87 kA  $I_p$  spike in case 3.0.

Contours of the  $n = 0$  toroidal current density at the time of current minimum and current maximum, as well as the  $n = 1$  current density at the time of the  $n = 1$  mode peak (occurring between the other two times), are compared for cases 1.0 and 3.0 (Fig. 12). The  $n = 0$  current density distribution changes significantly as the plasma current increases. At the time of the local minimum, the core of the plasma has very little current density, and the forward (positive) current density is peaked in an annular ring surrounding the core and extends outward to the separatrix. The region of forward current is surrounded by a ring of reversed current at the edge. The radial parallel current density profiles are also compared for all three cases at the  $I_p$  minima and maxima in Fig. 13. The current density profiles near the center at both times are less peaked and extend more toward the core for the pellets releasing their payloads further out. We might expect the current density to extend further inward when the payload is more concentrated in the core but recall that when the payload is released further out—over a larger volume of flux—the payload region does not initially cool to  $\sim 1$  eV, and only gradually does a very cold region appear in the center that strongly excludes current density. This region is narrower than the strongly cooled region with the more concentrated payload.

The reversed current ring was also seen in Ref. 22 and was interpreted in terms of the “flux-trapping” model proposed by Wesson,<sup>33</sup> in which poloidal flux is pushed outward and then trapped in the still-warm edge during the initial current redistribution, producing the reversed current region that disappears only when the edge cools and the trapped poloidal flux is released, leading to a plasma current spike. However, in the scenario considered by Wesson, the plasma is also warm in the core, and so poloidal flux dissipation at the o-point is not considered. During the plasma current spike in these simulations, the core is already cooled to just a few eV, but a warm edge region of hundreds of eV persists up to the time of the current local minimum, and the temperature in that region subsequently drops to only a few eV as the  $I_p$ -spike commences. As the negative current ring disappears, the forward current region expands outward and extends down to the divertor strike points, producing a halo current region. The halo current level is similar in each case. A surface integral of the current coming out of the wall at the outer strike point yields 120 kA, but about 50 kA flows back into the wall over a region around the outer-midplane, so that the current flowing into the wall near the inner strike-point is just 70 kA. Thus, a corresponding experimental halo current measurement of the return current flowing through the divertor would be 70 kA. However, these simulations are not expected to

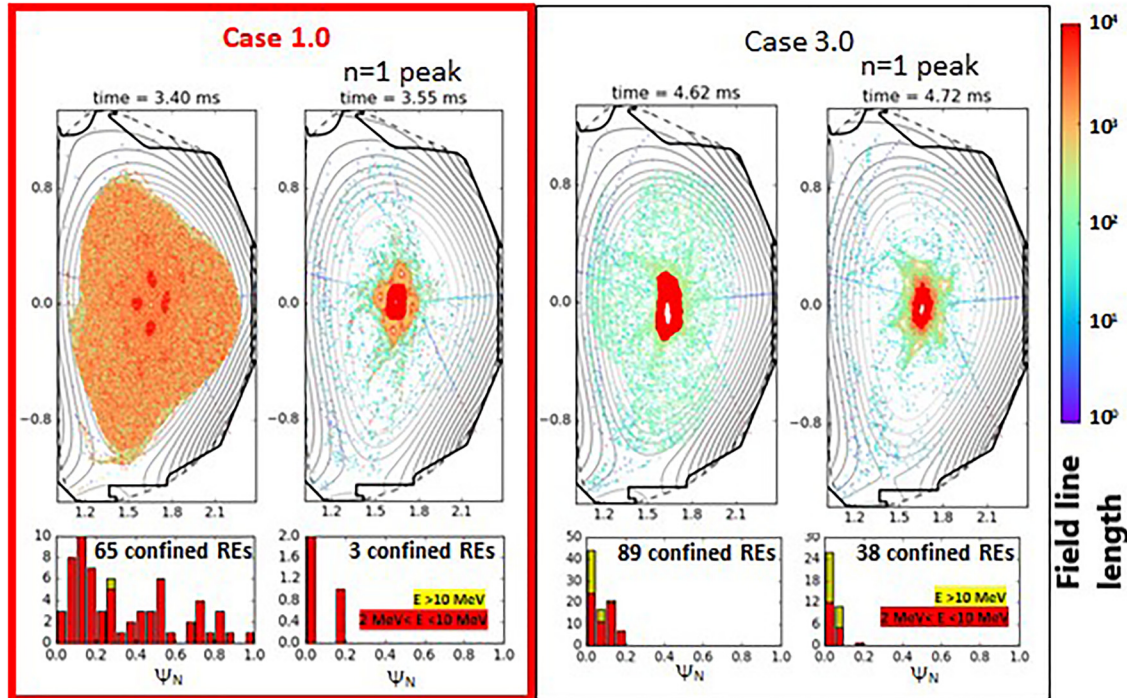


**FIG. 11.** Before the  $n = 1$  mode peak, case 3.0 retains a concentration of REs in the core on a small closed-flux region. Comparison of magnetic field topology and RE confinement for cases 1.0 (left) and 3.0 (right). (Upper) magnetic field line Poincaré plots at times of  $\sim 100$  REs, and  $n = 1$  peak. Field lines are color coded by number of toroidal transits before striking the wall, with 10 000 being the maximum integration length. (Lower) stacked histogram of RE distribution vs normalized poloidal flux (red: 2–10 MeV, yellow:  $> 10$  MeV, no REs  $< 2$  MeV are present at these times).

produce accurate halo-current predictions, both because these are ideal wall simulations ( $dB_n/dt = 0$ ) and also because no additional boundary conditions are imposed on the current into the wall, such as sheath boundary conditions that may be needed for accurate halo-current predictions.<sup>34</sup>

The  $n = 1$  mode associated with this event has a radially broad mode structure extending from the inner forward current ring to the outer reversed ring. Poloidally, the dominant mode numbers are  $m = 4$  (peaked near the inner current ring) and  $m = 3$  (with a broad radial extent). Although the evolution is well into the phase of nonlinear dynamics by the time that the final  $n = 1$  mode growth begins, we can obtain some insight into this mode by examining the safety factor profile evolution beginning before the last local minimum in the  $n = 1$  mode amplitude and continuing through the final growth phase and the  $I_p$  spike [Figs. 12(g) and 12(h)]. Both while the  $n = 1$  amplitude is still decaying and when it begins to grow again, a pair of  $q = 3$  surfaces exists, with one near the equilibrium  $q = 3$  surface, and one closer to the core. Just inside the inner  $q = 3$  surface is a  $q = 4$  surface. Prior to the start of the final  $n = 1$  growth, a pair of  $q = 2$  surfaces is also present between the  $q = 3$  surfaces. The mode begins to grow at approximately the time that the  $q = 2$  surfaces disappear as the inner  $q = 3$  surface moves outward, establishing a region of low magnetic shear between the  $q = 3$  surfaces. The flat profile near  $q = 3$  becomes more pronounced as the  $I_p$  local minimum is approached. Between the minimum and maximum  $I_p$ , the edge  $q$  rises quickly to around 4. Regarding the current spike, these simulations differ only in the details, with the qualitative phenomena virtually identical.

The  $q$ -profile taken together with the non-local radial structure of the mode is very suggestive of an  $m = 3/n = 1$  double tearing mode.<sup>35</sup> Unlike a standard tearing mode, this non-local structure can facilitate flattening of the current profile over a wide region of the edge. Notably, the double tearing mode has the same non-localized radial displacement  $\xi_r(r)$  as the  $m = 1$  tearing mode,<sup>35</sup> which is involved in flattening the central current density for outside-in thermal quench scenarios. In the DIII-D experiments, no analysis of the MHD fluctuation spectrum has been reported. We do note an experimentally similar scenario involving both a comparable  $q$ -profile with reversed magnetic shear and a hollow pressure profile that was reported on Alcator C-Mod during current ramp up.<sup>36</sup> In that case, linear stability analysis found both an  $m = 3$  double tearing mode and an  $m = 4$  resistive interchange localized to the inner  $q = 4$  surface, which was unstable not due to high  $\beta_N$  but due to the hollow pressure profile.

Dissipation of poloidal flux at the o-point can be observed in the time traces of total poloidal flux in Fig. 14. Each simulation undergoes a brief period of rapid dissipation of poloidal flux after the payload release, but this is considerably delayed in case 3.0 because the core temperature initially plateaus at a couple hundred eV and only later drops to the few eV range. During this interval, current density in the core is diffusing outward but not being dissipated at the o-point. By the start of the  $I_p$  spike, more poloidal flux has been dissipated for case 1.0, which is in competition with poloidal flux that is pushed outward and “trapped” at the edge. A reconnection event occurs at the time of the  $I_p$  spike to release the trapped poloidal flux. This can be observed by the drop in separatrix flux without a corresponding drop in total

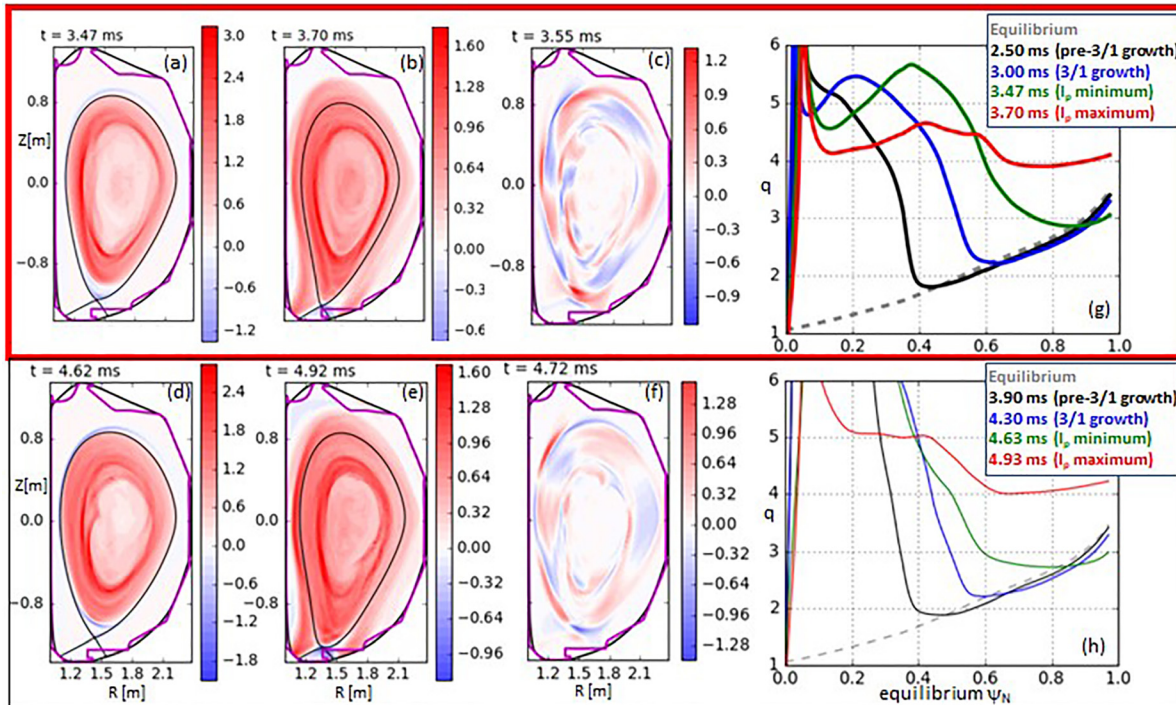


**FIG. 12.** A 3/1 double tearing mode redistributes the current density at the time of the  $I_p$ -spike. (a)–(f) Contours of toroidal current density ( $\text{MA}/\text{m}^2$ ). Case 1.0 (upper row):  $n = 0$  current density at (a) current local minimum and (b) current local maximum, and (c)  $n = 1$  current density at  $n = 1$  peak (between the other two times). Case 3.0 (lower row): (d)  $n = 0$  current density at (d) current local minimum and (e) current local maximum, and (f)  $n = 1$  current density at  $n = 1$  peak. (g) and (h) Safety factor profiles before and after the 3/1 mode begins to grow and at the current minima and maxima, as well as the equilibrium profile for case 1.0 (g) and case 3.0 (h).

flux, implying an increase in open flux surrounding the equilibrium—seen to occur at approximately the same time as the increase in plasma current. The effect of the reconnection event is also seen in plots of the separatrix shapes [Figs. 14(a) and 14(b)] at the times of the current local minimum and local maximum, clearly showing the downward

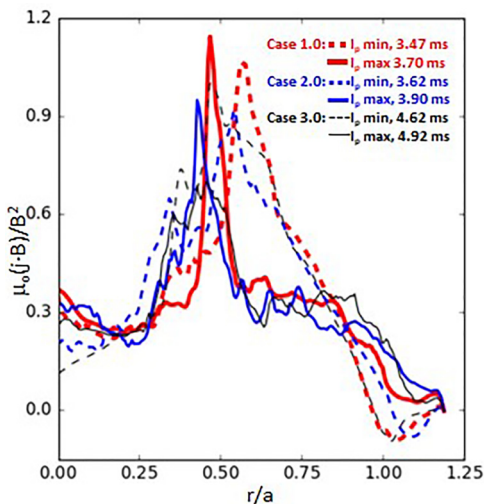


**FIG. 13.** The parallel current density profile at the outer-midplane at the times of the current local minima and the peak of the plasma current spike for all three cases.

movement of the x-point and the reduction of the closed flux volume. In every case, the current density in the outer half of the plasma becomes much flatter following the reconnection, with the negative current region near the boundary becoming positive and the current density just inside of that decreasing (Fig. 13). However, flattening of the current density profile does not extend to the magnetic axis. The exclusion of current density from the cold center inhibits the flattening of the profile in the core, especially in case 1.0 with the most concentrated payload. So for the fastest pellet scenario, two factors explain the smaller plasma current spike. First, the faster central cooling and greater dissipation of poloidal flux,  $\psi_{pol}$ , (without a significant change in plasma current) reduces the internal inductance before the spike ( $\psi_{pol} \propto I_t I_p$ ); and second, further drop in internal inductance due to profile flattening is partially inhibited by a larger impurity density in the center.

The destruction of flux surfaces associated with the  $n = 1$  mode peak was already plotted in Fig. 11. Poincaré plots for additional times as late as 1 ms after the  $I_p$  spike appear in Fig. 15 to show to the gradual reformation of flux surfaces beginning from the core. Although the field-line length before exiting the domain (indicated by field-line color) does increase over this 1 ms interval, stochasticity over much of the domain persists for a longer time.

**E. Variation of parameters**

For both the 230 m/s pellet and the 115 m/s pellet, scans of viscosity were carried out ranging over a factor of four in the former case,

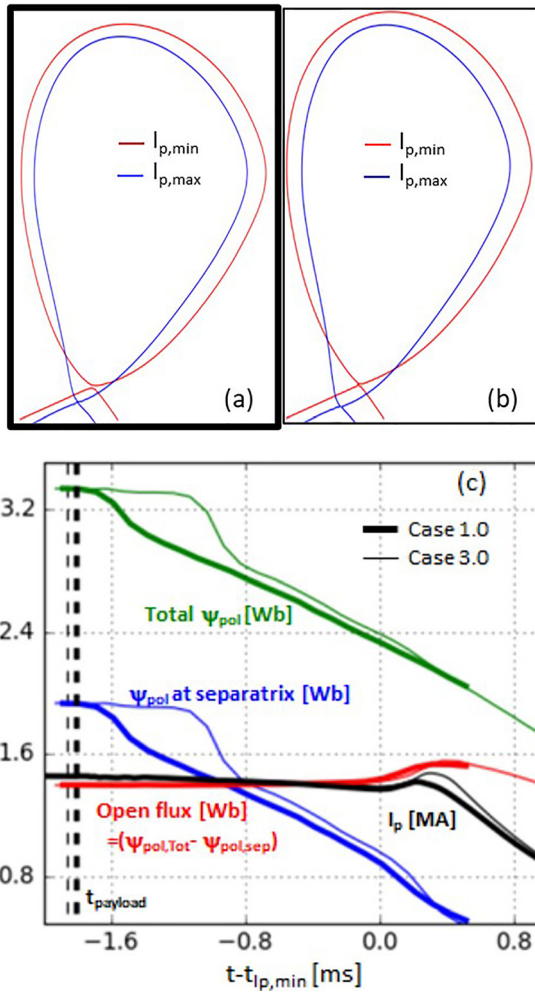


**FIG. 14.** The plasma current spike is associated with a reconnection event at the x-point. Comparison of separatrix shapes at current local minima and maxima for cases (a) 1.0 and (b) 3.0. (c) Time traces of maximum poloidal flux at the boundary, poloidal flux at the separatrix, open flux (the difference of previous two), and plasma current for cases 1.0 and 3.0, shifted by the time when the current spike begins (current local minimum). Time of payload release is indicated by the dashed vertical lines.

and two in the latter. Over this range of viscosity values, the simulations are remarkably unchanged. In fact, for the early phase of the simulation, plots of  $n=1$  mode amplitude and total radiated power overlay almost identically (Fig. 16). Later in the simulation, as the  $n=1$  mode grows large, some difference can be seen as viscosity is varied, but the quantitative similarity, even to the level of small fluctuations, is still quite pronounced. One difference that must be noted concerns the confinement of the last 0.1% of RE test particles. When viscosity is reduced to  $260 \text{ m}^2/\text{s}$  with the 230 m/s pellet, a small residual RE population is retained in the CQ, similar to the slower pellets, due to small changes to stochasticity in the core. However, when viscosity is further reduced to  $130 \text{ m}^2/\text{s}$ , the last of the RE test-particles is lost earlier than in the highest viscosity simulation. With test-particle counts in the single digits, clearly, assessing RE confinement in this

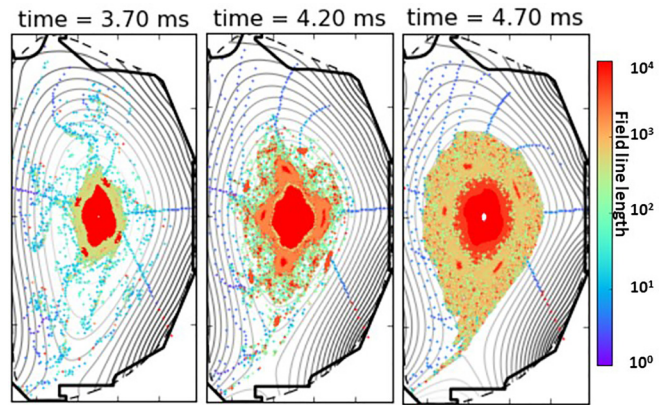


**FIG. 15.** Flux surfaces begin to re-heal slowly after the plasma current spike. Magnetic field Poincare plots are shown for case 1.0 at the time of the  $I_p$  spike as well as 0.5 and 1.0 ms later. Field lines are color coded by the number or toroidal transits before exiting the simulation domain, where 10 000 is the maximum integration length.

phase suffers from a problem of statistics. The lower viscosity case at 115 m/s retains a slightly larger number of REs than at higher viscosity. It is nevertheless noted that the range of viscosity values considered does not extend down to physically realistic values, with the large values required for reasons of numerical stability. Even with no significant changes in the mode growth observed over a factor of four in viscosity, a further reduction by two orders of magnitude could reveal additional MHD activity that is strongly damped in the present simulations.

Reduction of the Gaussian width of the source in the poloidal plane had a more dramatic effect on the simulation results. An additional simulation at 115 m/s pellet speed was carried out with a poloidal source width reduced by a factor of two (a factor of four reduction

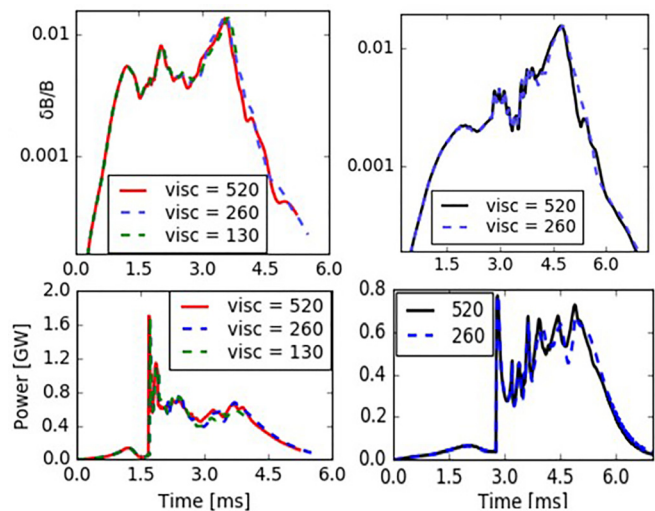


**FIG. 16.** A comparison of  $n=1$  mode amplitude (upper row) and radiated power (lower row) for simulations with different values of viscosity ( $\text{m}^2/\text{s}$ ). (Left) cases 1.0, 1.1, and 1.2; (right) cases 3.0 and 3.1.

in area and increase in peak density). The ablation curve for this simulation (case 3.2) was plotted in Fig. 4. The effect that the more concentrated impurity source has on the local ablation rate is extremely slight early in the shell ablation phase, up to  $r/a$  of 0.65. However, the pre-TQ MHD has a different character in this case. In the other cases, the destabilized 1/1 mode shifts the hot core away from the pellet and reduces the ablation prior to payload release. In case 3.2, a 2/1 mode grows, and then a stochastic region at mid-radius develops that enhances heat flux to the pellet by parallel transport and increases the ablation rate. This results in payload release at  $r/a = 0.54$  instead of  $r/a = 0.39$  (a difference of more than the payload delivery width). After this, a qualitatively different simulation unfolds. The localized deposition produces overall similar global radiation levels to the broader deposition, so the two effects that most likely to contribute to the destabilization of the 2/1 mode are the steeper temperature and current gradients produced by the narrower radial deposition and the more localized helical perturbation at the rational surfaces produced by the narrower poloidal deposition. Without presenting all the further details of this additional simulation, we can take away some important points from this result. First, the well-matched ablation rates in the early phase suggests that a theoretical ablation model, or one calibrated to experimental results, should be a decent predictive model regardless of the details of the source localization *provided the quantity of shell material deposited is low enough to avoid triggering pre-TQ MHD*. Every case modeled here has some pre-TQ MHD, but the goal of DSP is to use an almost non-perturbative shell. This may be easier to achieve in larger tokamaks using larger pellets at higher speeds where the payload-to-shell mass ratio could decrease roughly with the surface-to-volume ratio. Thus, for high shell quantities, such as the actual DIII-D quantities modeled here, the presence of unstable MHD in the pre-TQ makes the shell ablation difficult to predict, but as we extrapolate to larger devices, a predictive model may become more feasible.

#### IV. SUMMARY AND CONCLUSIONS

The set of simulations presented here were carried out with the primary aim of reproducing and offering additional insight into various trends observed in the DIII-D DSP velocity scan described by Hollmann.<sup>7</sup> Three observed trends were broadly reproduced. First, mitigation improved with increasing pellet speed. The experiment saw decreased divertor heat fluence, while the simulations show a trend of increasing radiated power fraction, with the fastest pellet achieving the ITER target of  $>90\%$ .<sup>1</sup> This trend can be understood simply in terms of more direct radiation of core thermal energy coupled with less perturbation of the edge from shell material as the pellet travels faster and penetrates deeper. The second reproduced experimental trend is the decrease in plasma-current-spike amplitude as pellet speed increases. Whereas the experiment produced a more step-like trend, an essentially linear relationship was found in the simulations (despite the quite step-like trend in payload release location). As we have observed, the growth of unstable MHD modes in the pre-TQ can make the exact payload delivery location hard to predict as a function of velocity and may subsequently impact how other parameters vary. The  $I_p$ -spike results from flattening of the parallel current density profile in the edge by a 3/1 double tearing mode, which becomes unstable once the local minimum in  $q$  exceeds 2 and produces a large stochastic region across the edge. The smaller  $I_p$ -spike for faster pellets is explained in terms of the dissipation of more poloidal flux at the magnetic axis

prior to the reconnection that expels poloidal flux at the x-point and due to less reduction of the current density peaking in the core where the plasma is strongly cooled by the payload. Third, the evolution of the core temperature profiles in the simulations is shown to be wholly consistent with the appearance of RE seeds only in the case of the fastest pellet, as was observed in the HXR prompt-loss signal. RE seed losses in these simulations, under the assumption that seeds occur over the whole closed flux region, range between  $\sim 99.9\%$  and  $100\%$ , which would not itself be expected to produce a noticeable variation in the measurement.

We note one trend reported in Ref. 7 that is definitely not reproduced: shorter CQ times with increasing pellet velocity. On the contrary, in Fig. 3, the 230 m/s pellet appears to produce the slowest current decay. The slow current decay for a slow pellet that is plotted in the experimental reference is clearly not a simple exponential decay; rather it has a series of bumps possibly indicative of additional MHD events during the CQ. If the slow pellet payload is released even further from the center radially, leaving a warm remnant region in the center, this could be one explanation for such behavior, but this is merely speculation. This discrepancy will be left to future study.

Some additional trends seen in the simulations that are not favorable to the DSP concept are higher peak radiation and higher radiation asymmetry for the fastest pellet. On the latter point, it is noted that the simulations are not considered to be predictive of the true asymmetry, rather it is largely governed by the choice of the neutral source asymmetry. However, both of these problems might be addressed in DSP experiments by choosing a payload designed to radiate more slowly, for instance with large sized grains that take some time to ablate as they disperse; as noted in Ref. 7, considerable optimization of the concept is still possible.

Although the RE confinement results show a monotonic trend of increasing loss with increasing pellet speeds, the statistics in the range of difference between the cases were poor, and the results were modified by varying viscosity. A very high loss fraction is seen in every case, but for a high current machine with a large avalanche multiplication, a loss fraction of 99.9% may still be too low. Total loss of RE seeds appears to rely both on destruction of core flux surfaces by a payload centered near the o-point, and destruction of edge flux surfaces by a reconnection event at the x-point. We conclude that statistics need to be improved with more test particles to understand trends in the simulations, and that scenarios that increase flux-surface destruction in the core should be devised if possible. Whether similar levels of loss could be achieved in ITER is very much an open question in light of previous modeling.<sup>13</sup>

Parameter scans indicate that the simulations are not particularly sensitive to viscosity over the range considered, and that the direct effect of a more localized source on the nearby plasma does not strongly affect the ablation rate. Changes in unstable MHD mode growth produced by changes in source localization, however, can significantly impact ablation. Since the aim of DSP is to use a non-perturbative shell and avoid pre-TQ MHD, a predictive model should be possible in a better optimized scenario. In addition to the variation of viscosity and poloidal source localization, some initial attempts were made to reduce toroidal localization and the payload deposition width (for the slower pellets), and to include temperature dependent thermal conduction. All these attempts resulted in numerically unstable simulations at the resolutions attempted. Prior DSP simulations

with a more toroidally peaked source<sup>22</sup> were performed with a cutoff value for the minimum resistivity, and some trade-off in parameter space seems to be necessary for a given resolution. Larger simulations with increased poloidal and toroidal resolution will be required to push all parameters toward more realistic values.

## ACKNOWLEDGMENTS

The author thanks C.C. Kim for valuable suggestions on this manuscript. This material is based upon work supported by the Department of Energy under Award Nos. DE-FG02-95ER54309 and DE-FC02-04ER54698. This research used resources of the National Energy Research Scientific Computing Center (NERSC), a U.S. Department of Energy Office of Science User Facility operated under Contract No. DE-AC02-05CH11231. Part of the data analysis was performed using the OMFIT integrated modeling framework.<sup>37</sup>

This report was prepared as an account of work sponsored by an agency of the United States Government. Neither the United States Government nor any agency thereof, nor any of their employees, makes any warranty, express or implied, or assumes any legal liability or responsibility for the accuracy, completeness, or usefulness of any information, apparatus, product, or process disclosed, or represents that its use would not infringe privately owned rights. Reference herein to any specific commercial product, process, or service by trade name, trademark, manufacturer, or otherwise does not necessarily constitute or imply its endorsement, recommendation, or favoring by the United States Government or any agency thereof. The views and opinions of authors expressed herein do not necessarily state or reflect those of the United States Government or any agency thereof.

## DATA AVAILABILITY

The data that support the findings of this study are available from the corresponding author upon reasonable request.

## REFERENCES

- <sup>1</sup>M. Lehnen, K. Aleynikova, P. B. Aleynikov, D. J. Campbell, P. Drewelow, N. W. Eidietis, Y. Gasparyan, R. S. Granetz, Y. Gribov, N. Hartmann, E. M. Hollmann, V. A. Izzo, S. Jachmich, S.-H. Kim, M. Kočan, H. R. Koslowski, D. Kovalenko, U. Kruezi, A. Loarte, S. Maruyama, G. F. Matthews, P. B. Parks, G. Pautasso, R. A. Pitts, C. Reux, V. Riccardo, R. Rocella, J. A. Snipes, A. J. Thornton, and P. C. De Vries, *J. Nucl. Mater.* **463**, 39–48 (2015).
- <sup>2</sup>N. Commaux, L. R. Baylor, T. C. Jernigan, E. M. Hollmann, P. B. Parks, D. A. Humphreys, J. C. Wesley, and J. H. Yu, *Nucl. Fusion* **50**, 112001 (2010).
- <sup>3</sup>S. H. Park, K. S. Lee, L. R. Baylor, S. J. Meitner, H. M. Lee, J. I. Song, T. E. Gebhart, S. W. Yun, J. Kim, K. P. Kim, K. R. Park, and S. W. Yoon, *Fusion Eng. Des.* **154**, 111535 (2020).
- <sup>4</sup>Y. Li, Z. Y. Chen, Y. N. Wei, R. H. Tong, W. Yan, Z. F. Lin, Z. J. Yang, and Z. H. Jiang, *Rev. Sci. Instrum.* **89**, 10K116 (2018).
- <sup>5</sup>H. B. Xu, G. L. Zhu, Z. Cao, Y. B. Dong, Y. K. Zhong, X. Cai, L. Liu, Y. G. Li, Z. C. Yang, J. Wang, P. Lu, and D. Q. Liu, *Fusion Sci. Technol.* **76**, 857–860 (2020).
- <sup>6</sup>U. Losada, A. Manzanares, I. Balboa, S. Silburn, J. Karhunen, P. J. Carvalho, A. Huber, V. Huber, E. R. Solano, and E. de la Cal, *Nucl. Mater. Energy* **25**, 100837 (2020).
- <sup>7</sup>E. M. Hollmann, P. B. Parks, D. Shiraki, N. Alexander, N. W. Eidietis, C. J. Lasnier, and R. A. Moyer, *Phys. Rev. Lett.* **122**, 65001 (2019).
- <sup>8</sup>V. A. Izzo, *Nucl. Fusion* **46**, 541 (2006).
- <sup>9</sup>V. A. Izzo, D. G. Whyte, R. S. Granetz, P. B. Parks, E. M. Hollmann, L. L. Lao, and J. C. Wesley, *Phys. Plasmas* **15**, 056109 (2008).
- <sup>10</sup>V. A. Izzo, P. B. Parks, N. W. Eidietis, D. Shiraki, E. M. Hollmann, N. Commaux, R. S. Granetz, D. A. Humphreys, C. J. Lasnier, R. A. Moyer, C. Paz-Soldan, R. Raman, and E. J. Strait, *Nucl. Fusion* **55**, 073032 (2015).
- <sup>11</sup>V. A. Izzo, *Phys. Plasmas* **20**, 056107 (2013).
- <sup>12</sup>D. Shiraki, N. Commaux, L. R. Baylor, N. W. Eidietis, E. M. Hollmann, V. A. Izzo, R. A. Moyer, and C. Paz-Soldan, *Nucl. Fusion* **55**, 073029 (2015).
- <sup>13</sup>V. A. Izzo, E. M. Hollmann, A. N. James, J. H. Yu, D. A. Humphreys, L. L. Lao, P. B. Parks, P. E. Sieck, J. C. Wesley, R. S. Granetz, G. M. Olynyk, and D. G. Whyte, *Nucl. Fusion* **51**, 063032 (2011).
- <sup>14</sup>N. M. Ferraro, B. C. Lyons, C. C. Kim, Y. Q. Liu, and S. C. Jardin, *Nucl. Fusion* **59**, 16001 (2019).
- <sup>15</sup>B. C. Lyons, C. C. Kim, Y. Q. Liu, N. M. Ferraro, S. C. Jardin, J. McClenaghan, P. B. Parks, and L. L. Lao, *Plasma Phys. Controlled Fusion* **61**, 64001 (2019).
- <sup>16</sup>D. Hu, E. Nardon, M. Hoelzl, F. Wieschollek, M. Lehnen, G. T. A. Huijsmans, D. C. van Vugt, S.-H. Kim, JET Contributors, and JOE team, *Nucl. Fusion* **61**, 026015 (2021).
- <sup>17</sup>C. Sommariva, E. Nardon, P. Beyer, M. Hoelzl, G. T. A. Huijsmans, and D. Van Vugt, *Nucl. Fusion* **58**, 016043 (2018).
- <sup>18</sup>M. Hoelzl, D. Hu, E. Nardon, and G. T. A. Huijsmans, *Phys. Plasmas* **27**, 022510 (2020).
- <sup>19</sup>C. C. Kim, Y. Q. Liu, P. B. Parks, L. L. Lao, M. Lehnen, and A. Loarte, *Phys. Plasmas* **26**, 42510 (2019).
- <sup>20</sup>E. Nardon, A. Fil, M. Hoelzl, and G. Huijsmans, *Plasma Phys. Controlled Fusion* **59**, 014006 (2017).
- <sup>21</sup>V. A. Izzo and P. B. Parks, *Phys. Plasmas* **24**, 060705 (2017).
- <sup>22</sup>V. A. Izzo, *Nucl. Fusion* **60**, 066023 (2020).
- <sup>23</sup>C. R. Sovinec, A. H. Glasser, T. A. Gianakon, D. C. Barnes, R. A. Nebel, S. E. Kruger, S. J. Plimpton, A. Tarditi, M. S. Chu, and NIMROD Team, *J. Comput. Phys.* **195**, 355 (2004).
- <sup>24</sup>D. G. Whyte, T. E. Evans, A. G. Kellman, D. A. Humphreys, A. W. Hyatt, T. C. Jernigan, R. L. Lee, S. L. Luckhardt, P. B. Parks, M. J. Schaffer, and P. L. Taylor, “Energy balance, radiation and stability during rapid plasma termination via impurity pellet injections on {{DIII-D}},” in *Proceedings of the 24th European Conference on Controlled Fusion and Plasma Physics* (European Physical Society, Berchtesgaden, Germany, 1997), p. 1137.
- <sup>25</sup>See ADAS Project, [https://doi.org/https://open.adas.ac.uk/element/detail/adf11/plt89/plt89\\_b.dat](https://doi.org/https://open.adas.ac.uk/element/detail/adf11/plt89/plt89_b.dat) for the data file “PLT Line Emission from Excitation”
- <sup>26</sup>See ADAS Project, [https://doi.org/https://open.adas.ac.uk/element/detail/adf07/ionelec/ionelec\\_szd\[b.dat](https://doi.org/https://open.adas.ac.uk/element/detail/adf07/ionelec/ionelec_szd[b.dat) for the data file “Electron Impact Ionization”
- <sup>27</sup>H. P. Summers, M. G. O’Mullane, A. D. Whiteford, N. R. Badnell, and S. D. Loch, “ADAS: Atomic data, modelling and analysis for fusion,” *AIP Conf. Proc.* **901**, 239–248 (2007).
- <sup>28</sup>P. B. Parks and R. J. Turnbull, *Phys. Fluids* **21**, 1735 (1978).
- <sup>29</sup>H. Dreicer, *Phys. Rev.* **115**, 238 (1959).
- <sup>30</sup>H. M. Smith and E. Verwichte, *Phys. Plasmas* **15**, 72502 (2008).
- <sup>31</sup>E. M. Hollmann, N. Commaux, R. A. Moyer, P. B. Parks, M. E. Austin, I. Bykov, C. Cooper, N. W. Eidietis, M. O’Mullane, C. Paz-Soldan, D. L. Rudakov, and D. Shiraki, *Nucl. Fusion* **57**, 16008 (2017).
- <sup>32</sup>H. E. Mynick and J. D. Strachan, *Phys. Fluids* **24**, 695 (1981).
- <sup>33</sup>J. A. Wesson, D. J. Ward, and M. N. Rosenbluth, *Nucl. Fusion* **30**, 1011 (1990).
- <sup>34</sup>F. J. Artola, A. Loarte, E. Matveeva, J. Havlicek, T. Markovic, J. Adamek, J. Cavalier, L. Kripner, G. T. A. Huijsmans, M. Lehnen, M. Hoelzl, and R. Panek, *Plasma Phys. Controlled Fusion* **63**, 64004 (2021).
- <sup>35</sup>P. L. Pritchett, Y. C. Lee, and J. F. Drake, *Phys. Fluids* **23**, 1368 (1980).
- <sup>36</sup>Y. In, J. J. Ramos, A. E. Hubbard, I. H. Hutchinson, M. Porkolab, J. Snipes, S. M. Wolfe, and A. Bondeson, *Nucl. Fusion* **40**, 1463 (2000).
- <sup>37</sup>O. Meneghini, S. P. Smith, L. L. Lao, O. Izacard, Q. Ren, J. M. Park, J. Candy, Z. Wang, C. J. Luna, V. A. Izzo, B. A. Grierson, P. B. Snyder, C. Holland, J. Penna, G. Lu, P. Raum, A. McCubbin, D. M. Orlov, E. A. Belli, N. M. Ferraro, R. Prater, T. H. Osborne, A. D. Turnbull, and G. M. Staebler, *Nucl. Fusion* **55**, 083008 (2015).